Tuning critical resolved shear stress ratios for BCC-Titanium Ti21S via an automated data analysis approach

Kaustubh Venkatraman, Meriem Ben Haj Slama, Vincent Taupin, Nabila Maloufi, Antoine Guitton

Tuning critical resolved shear stress ratios for BCC-Titanium Ti21S via an automated data analysis approach

Kaustubh Venkatraman[1,2], Meriem Ben Haj Slama[1,2] ,Vincent Taupin[1,2], Nabila Maloufi[1,2], Antoine Guitton[1, 2,*]

[1] Université de Lorraine – CNRS – Arts et Métiers ParisTech – LEM3, France

[2] Labex Damas – Université de Lorraine, France

*Corresponding author: Université de Lorraine – CNRS – Arts et Métiers ParisTech – LEM3
7 rue Félix Savart, 57070 Metz – France
antoine.guitton@univ-lorraine.fr
Phone: +33 372 747 787

ABSTRACT

We introduce a novel method for automated slip trace detection and analysis based on the Hough transform algorithm and apply it to Electron Channelling Contrast Imaging micrographs. This is further augmented with an automation procedure for the determination of slip-trace crystallography in conjunction with orientation data acquired via electron backscattered diffraction. Automation is required for faster indexation of the slip traces and for more reliable statistical studies. The automation procedure was applied to different regions of interest on a β-Ti21S sample loaded *in situ* in tension. β-Ti21S is a BCC alloy with 48 slip systems available to accommodate plastic deformation, including all complexities associated with pencil glide. Multiple regions of interest were analyzed using the automation procedure. The acquired slip distribution statistics reveals that the majority of the slip traces belong to the {112} and {123} slip families. The deformation response of the observed regions of interest was also simulated using a full-field crystal plasticity model implemented in DAMASK, based on a phenomenological power law based constitutive formulation, incorporating all potentially active 48 slip systems. The slip system activity distribution from modelling is compared with the slip distribution statistics observed experimentally. The plasticity parameters for β-Ti21S were taken from the literature and the Critically Resolved Shear Stress (CRSS) values were adjusted to match the experimentally observed yield stress value. We begin with uniform CRSS ratios for all three potential slip system families and tune the CRSS ratios to match the slip-distribution statistics experimentally, keeping the average CRSS value the same for all cases. Thus, a method has been introduced to tune average CRSS values and ratios by considering both the macroscopic stress-strain response and the locally observed slip-distribution statistics, obtained via automated slip trace detection procedure.

Keywords: *In situ* tensile test; slip trace analysis, Full-field Crystal plasticity modelling; ECCI; β-Ti21S.

1 Introduction

Crystal plasticity modelling is a powerful tool to gain insights into the dependence of mechanical properties on the microstructural features of crystalline materials. The description of internal micro-structure exists at different length scales, ranging from the atomic level description of defects to micron sized features such as slip-lines and grain boundaries to macroscopic textures of polycrystalline metals. Advances in instrumentation and experimental techniques have progressively led to a refinement of the microstructural information available at sub-micron length scales. This has been accompanied by a parallel development in the mechanistic description at these length scales and the successful integration of multi-physics modules in a hierarchical format by different micro-mechanical modelling tools [1], [2]. Analytical homogenization theories, traditionally applied as mean-field effective response of statistically-defined classes of poly-crystals are being replaced by full-field models, which allow for the determination of the statistical distribution of micro-mechanical fields inside poly-crystalline materials [1]. The statistical description of the distribution of these micro-mechanical fields is becoming increasingly relevant due to concurrent advancements in experimental techniques that provide direct evidence for the heterogeneity and localization of such micro-mechanical fields at the nanometer scale, where dislocation mechanisms are active. The phenomenological description of elasto-plastic deformation is expressed via flow rules that involve various material parameters. For example, in a phenomenological power law description of poly-crystalline plasticity, first described by Hutchinson *et al.* [3] for FCC polycrystals, one of the parameters represents the dependence of shearing rates of different slip systems on the resolved shear stresses on these slip systems via the strain rate sensitivity exponent. The flow rule is typically expressed either by a power law, an exponential law or a hyperbolic sine type expression [4]–[6] for modelling

deformation by creep at elevated temperatures. There are other parameters that describe the interactions between different active slip systems and lead to macroscopic hardening behaviour [7], [8]. Parameter identification is generally carried out using a range of different experimental techniques available in the literature like nano-indentation experiments, micro-pillar compression experiments, strain maps from High Resolution Digital Image Correlation (HR-DIC) experiments, experiments on single crystals etc. [9]–[18]. These methods carried out at the grain scale are usually time consuming [15]. There is an increased effort towards utilizing local micro-mechanical fields such as HR-DIC strain maps or slip traces [19] for parameter identification. This is because modelling the macroscopic experimental stress-strain response for parameter identification does not always lead to a unique solution as multiple deformation states can be accommodated by the same macroscopic response [20]. Such coupled approaches can provide information on textures, Geometrically Necessary Dislocation (GND) density patterning, plastic strain localization and transfer across grain boundaries, etc. In particular, the increasing use of machine learning techniques [21], [22], genetic algorithms [15] and artificial neural networks [23] for capturing experimentally observed micro-mechanical response such as stress hotspots, micro-crack propagation, spatial strain localization etc. are becoming very popular. Among the results, such coupled modeling-experimental methods show importantly that it is possible to connect the evolution of microstructures to their stress-strain state and to fine-tune the modelling parameters to match the experimentally observed local deformation response.

The experimental approach adopted in the following study is based on Scanning Electron Microscopy (SEM) images of slip traces which are used for quantifying the local dislocation slip activity in a given region of interest. These images were obtained using the Electron Channeling Contrast Imaging (ECCI) technique, which offers the ability to

provide transmission electron microscopy-like diffraction contrast imaging of near-surface defects in bulk samples with a good accuracy. Moreover, ECCI enables a large area of view [24]–[29], thus providing relevant statistical information for comparison with the modelling procedure. An optimized procedure referred as Accurate Electron Channeling Contrast Imaging (A-ECCI), and based on the precise control of the channeling conditions taking advantage of the 0.1° angular resolution of High Resolution Selected Area Channeling Patterns with an improved spatial resolution of 500nm was developed some years ago [27], [28], [30], [31]. A-ECCI thus enables the comprehensive characterization of defects such as stacking faults or dislocations, and can be used in conjunction with *in situ* tensile test inside the SEM [32], [33]. This technique provides access to multiple regions of interest; from sample scale to dislocation scale; with one unique tool while loading a bulk sample, thus providing access to large datasets amenable to the application of data mining procedures. This technique also provides a clear contrast for resolving slip-lines in a large region of interest. This is quite useful in enumerating relevant statistical parameters from the description of microstructural features available at different length scales.

The material β-Ti21S with chemical composition Ti-15Mo-3Nb-3Al-0.2Si is a metastable titanium alloy with a body centered cubic (BCC) structure that was introduced in 1989 and designed for high temperature strength and creep resistance, good cold formability, good corrosion/oxidation resistance and thermal stability for applications up to 593°C, making it a suitable candidate material for aerospace applications and bio-medical implants [34]–[38]. For this study, *in situ* tensile tests were conducted on β-Ti21S. Slip-line images from multiple regions were acquired at the onset of plasticity. Field outputs from the full-field modelling procedure are compared with the experimental slip-line distribution in terms of slip system activities and accumulated plastic slip strain

distributions. For the majority of metals, dislocation and slip system activation at yield follows the well-known Schmid law, but BCC metals are reported to violate this law and show anomalous slip behavior as reported in many experimental studies [39]–[43]. More recent work proposed a modified parameter-free Schmid law to quantify the deviations from the Schmid law based on the deviations of the screw dislocation trajectory away from a straight path between equilibrium configurations [44]. This deviation from the Schmid law is a material dependent property and depends also on other aspects such as alloy composition, testing temperature and strain rate [45]. Furthermore, the number of activated slip systems in BCC metals can be as high as 24 or even 48, and pencil glide is frequently reported in experiments [46]–[49]. For these reasons, we choose a BCC metal as a challenging benchmark for our proposed experimental / theoretical strategy viz. β-Ti21S.

The experimental and modelling work that we describe below is driven by the following objectives, namely (*i*) to perform *in situ* tensile tests on a bulk Ti21S specimen, (*ii*) observation of slip traces and following their evolution during deformation using ECCI, (*iii*) development of an automation algorithm to detect slip traces, (*iv*) and determination of the crystallographic slip plane associated with the slip trace in conjunction with Electron Back Scattered Diffraction (EBSD) data for multiple points on the detected slip traces. This can be used further to quantify the distribution of slip activity amongst different active slip families in different regions of interest, *(v)* run full-field crystal plasticity simulations using EBSD-data based digitized microstructures of different regions of interest, based on the open-source Düsseldorf Advanced Materials Simulation Kit (DAMASK), *(vi)* collecting local simulated field outputs such as the accumulated plastic shear and quantifying the slip-family activity distributions in different regions based on these field outputs, *(vii)* tuning the critically resolved shear stress (CRSS) values

to match the slip family distribution observed via the automation procedure and thus to provide CRSS ratios between different slip families for describing the slip-family distribution observed experimentally.

2 Materials and experimental procedures

2.1 Sample preparation and mechanical testing:

The details of the experimental procedure and the mechanical testing have been detailed elsewhere [32] and briefly recapitulated here. The tensile sample was cut from a 1.78 mm thickness rolled sheet of β-Ti21S alloy, produced by Titanium Metals Corporation. The chemical composition of the material is Ti-15.9Mo-2.7Nb-2.9Al-0.2Fe-0.2Si. Tensile testing was performed at room temperature with a DEBEN micro-tensile testing machine. The tensile deformation was performed under an imposed initial strain rate of $3.3 \times 10^{-4}\,s^{-1}$. The sample was mechanically polished with 1 μm diamond paste, followed by chemo-mechanical polishing with colloidal silica suspension and subsequently ion-polished in a PECS II ion polishing system with a 3 keV beam. The *in situ* microstructural characterization during deformation, was performed by A-ECCI for a precise analysis of defects (Dislocations/Slip-lines), in a Zeiss Auriga Scanning Electron Microscope operating at 10 kV. EBSD based orientation mapping was carried out on the different regions of interest to provide grain orientation mapping to an accuracy of about 2° in a Zeiss Supra 40 SEM operating at 20 kV.

2.2 Procedure for detecting slip lines in the deformed region of interest and establishing the slip-family distribution statistics:

An automation procedure was set up in MATLAB to detect slip lines in a given region of interest consisting of multiple grains with the objective of tagging multiple lines by an index number, establishing the co-ordinates of the detected lines and the slope of the slip

line with respect to the tensile axis. The slope of the detected slip line would be compared with the possible slip traces of active slip families obtained through orientation maps from EBSD to determine the active slip-plane family closest to the detected slip trace. Section 2.2.1 outlines the details of the slip-line detection algorithm and Section 2.2.2 describes the procedure adopted for slip-plane family identification.

2.2.1 Automation procedure for slip line detection

The ECC micrographs were segmented to a binary format with a thresholding procedure available in Image-J [50], as shown in Figure 1, to highlight the slip lines in a given region of interest and to eliminate all other sources of contrast.

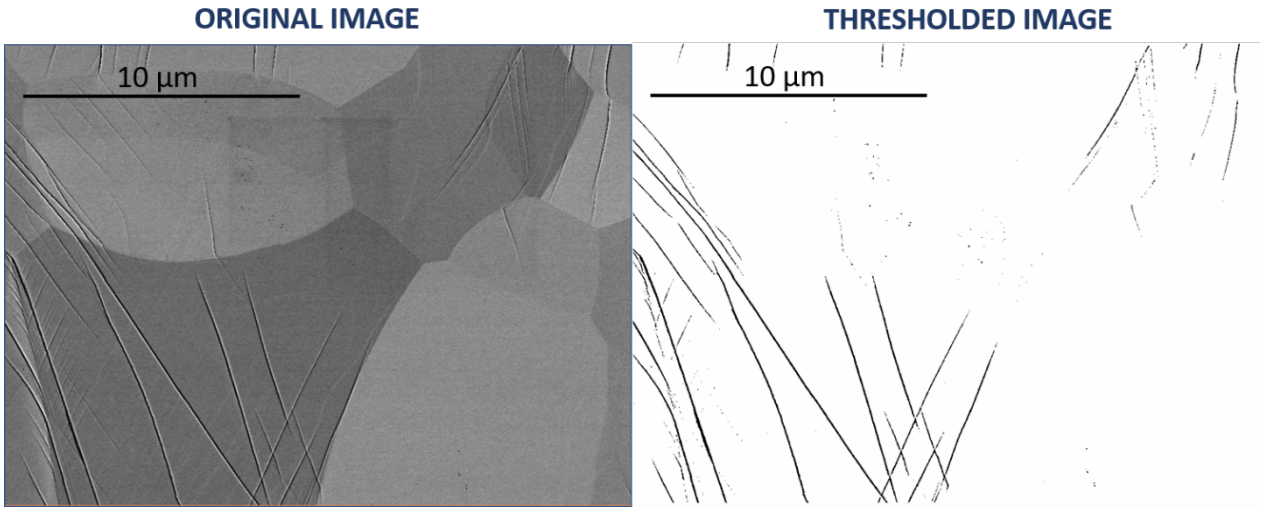

Figure 1: *ECC micrograph of a plastically deformed region of interest and its corresponding binary image used for the slip line detection algorithm.*

The thresholding procedure is necessary to make the edges of the slip lines visible to an edge detection operator. The edges corresponding to each line and their corresponding pixels (x,y) are detected using a 'Canny edge detection operator' available in MATLAB which utilizes the first order gradients of the binary image. Subsequently, the linear Hough transform algorithm [51] is used for detecting lines corresponding to these edges. which is achieved by parameterizing the cartesian space in the polar Hough space. The

edge coordinates in the image are known and therefore serve as constants in the parametric line equation, expressed in terms of unit vectors $\vec{\imath}$ & $\vec{\jmath}$ in the Cartesian space

$$\vec{r} = x\cos\theta \cdot \vec{\imath} + y\sin\theta \cdot \vec{\jmath} \quad (1)$$

where $\vec{r}$ and θ are the unknown variables we seek. For each edge pixel in the image with the position (x_i,y_i), infinitely many lines can pass through it. By using Equation 1 all these lines can be transformed into the Hough space, which gives a sinusoidal curve that is unique for that pixel. The same procedure when repeated for another neighbouring pixel gives another curve that intersects the first curve in one point, in the Hough space. This point represents the line, in the image space, that goes through both pixels. This can be repeated for all the pixel coordinates corresponding to the detected edges. When the Hough transform is made on the image for all the detected edge pixels, the lines passing through the maximum number of edge pixels can be found. The maximum number of pixels considered to be belonging to one line can be fixed on the basis of the minimum length of the line to detected. The result of the Hough transform is stored in a matrix that often called an accumulator [51]. One dimension of this matrix is the θ values and the other dimension is the $\vec{r}$ values, and each element has a value telling how many pixels lie on the line with the parameters $(\vec{r}, \theta)$. The element with the highest value indicates the line that is best represented in the input image.

When viewed in Hough parameter space, points which are collinear in the Cartesian image space become readily apparent as they yield curves with common intersection points as highlighted by the red boxes in Figure 2(ii). The Hough peaks function available in MATLAB is used to locate the peaks in the Hough transform matrix by specifying the number of peaks and the threshold value for detecting the minimum value to be considered as a peak. The Hough lines function is subsequently used to extract line segments from the binary image associated with the relevant Hough transform bins. The

Hough lines function allows us to specify the minimum line length to be detected and the minimum distance between two lines associated with the same Hough transform bin. Each detected line (highlighted in green) is indexed by a line number and the two end points are highlighted with red and blue, respectively, as shown in Figure 2(i). Once the end-points of the line are detected, co-ordinates for intermediate points can be extracted by iteratively finding the mid-points of the detected line segment. An example for finding the point co-ordinates corresponding to detected line divided into eight segments is shown in Figure 2(iii). In general, for a line with end points x_1, y_1 and x_2, y_2 , the k^{th} division will divide the line into 2^k segments and 2^{k-1} intermediate points. The general formula for the co-ordinates of the 2^{k-1} intermediate points following the k^{th} division, would be:

$$\frac{(2^k-1)x_1+(2^k-(2^k-1))x_2}{2^k}, \frac{(2^k-1)y_1+(2^k-(2^k-1))y_2}{2^k} \text{ for point 1}$$

$$\frac{(2^k-3)x_1+(2^k-(2^k-3))x_2}{2^k}, \frac{(2^k-3)y_1+(2^k-(2^k-3))y_2}{2^k} \text{ for point 2}$$

$$\frac{(2^k-5)x_1+(2^k-(2^k-5))x_2}{2^k}, \frac{(2^k-5)y_1+(2^k-(2^k-5))y_2}{2^k} \text{ for point 3}$$

.
.
.

$$\frac{(2^k-(2^k-1))x_1+(2^k-1)x_2}{2^k}, \frac{(2^k-(2^k-1))y_1+(2^k-1)y_2}{2^k} \text{ for the } 2^{k-1} \text{ point.}$$

The upper limit on the number of chosen intermediate points is based on the spatial resolution of the EBSD data. To compute the minimum number of points chosen on a given slip trace, we divide the length of the shortest slip trace as observed by ECCI by the scaling factor (number of pixels/unit length) as obtained from EBSD. This would be the minimum number of points that should be chosen for slip system identification. In our study, this number is around 9 points. For the three areas analyzed in the present study, n=9 is the upper limit for the number of points on the detected slip line without any overlapping for the points at which the measurements were made. The points will overlap

if the number of points chosen on a slip trace for slip system identification exceeds the number of pixels which constitute the slip trace, as per the EBSD resolution. The angle 'α_{expt}' (computed with respect to the loading direction) for all the points on a detected line, for each line, along with its pixel co-ordinates and label number are stored as an output, subsequent to the Hough transform.

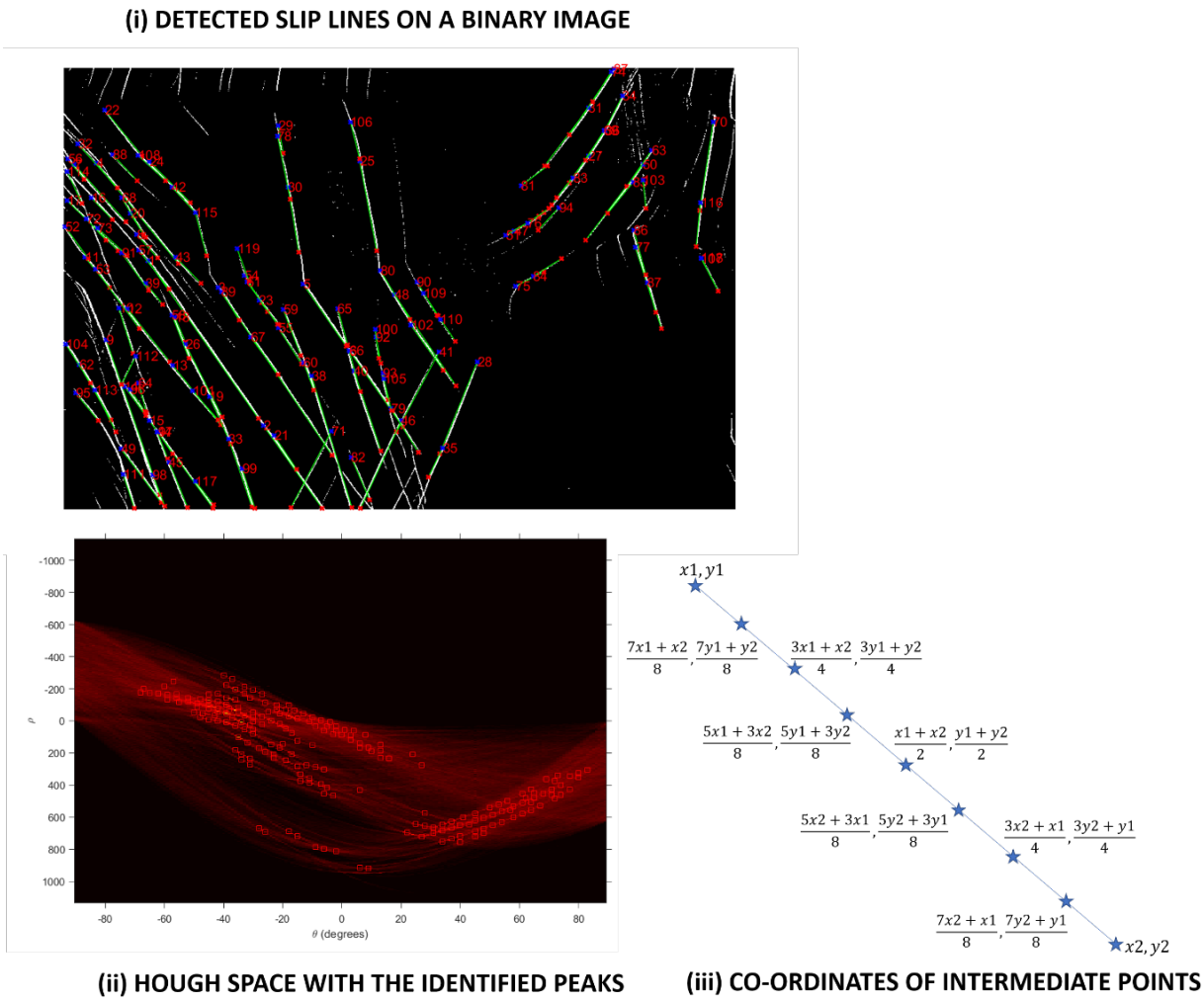

Figure 2: *Hough transform based automated slip line detection algorithm. (i) Detected slip lines highlighted in green marked by red and blue end points, (ii) Hough space representation of the binary image with identified peaks, (iii) co-ordinates for the intermediate points on a detected line, given the co-ordinates of the end-points.*

2.2.2 Procedure for determining the crystallography of slip for different points on the detected lines in conjunction with EBSD

With the EBSD map of the investigated zone all the theoretical plane traces corresponding to each plane family ({110}, {112}, {123}) were determined using ATEX software [52] as well as their associated angles (α_{EBSD}) with respect to the loading direction. These were computed at each pixel location within the EBSD (Figure 3 (b, c, d)). For all points corresponding to the detected lines using the automation algorithm, the angular difference ($|\alpha_{expt} - \alpha_{EBSD}|$) corresponding to the slip line angle and the theoretical angle of a given slip plane family is used to determine the most probable active slip plane family observed. The correlation co-efficient for each detected line, based on the angular difference is defined as follows:

$$\vec{R} = \begin{pmatrix} r_1 \\ r_2 \\ r_3 \end{pmatrix} = \begin{pmatrix} cos\left(min\left\{\left|\alpha_{expt} - \alpha_{EBSD}\right|_{110}\right\}\right) \\ cos\left(min\left\{\left|\alpha_{expt} - \alpha_{EBSD}\right|_{112}\right\}\right) \\ cos\left(min\left\{\left|\alpha_{expt} - \alpha_{EBSD}\right|_{123}\right\}\right) \end{pmatrix} \quad (2)$$

with

$$\left|\alpha_{expt} - \alpha_{EBSD}\right| \in \left[0, \frac{\pi}{2}\right].$$

and r_i (i = 1,2,3) corresponding to the {110}, {112} and {123} family of planes respectively.

For some of the detected lines, there can be an ambiguity in determining the most consistent slip plane family, as shown in Figure 3 (c) & (d). For slip line 1 shown in Figure 3 (a), it is clearly seen that there is an ambiguity in choosing between the {112} and {123} family of planes (Figure 3 (c,d)).

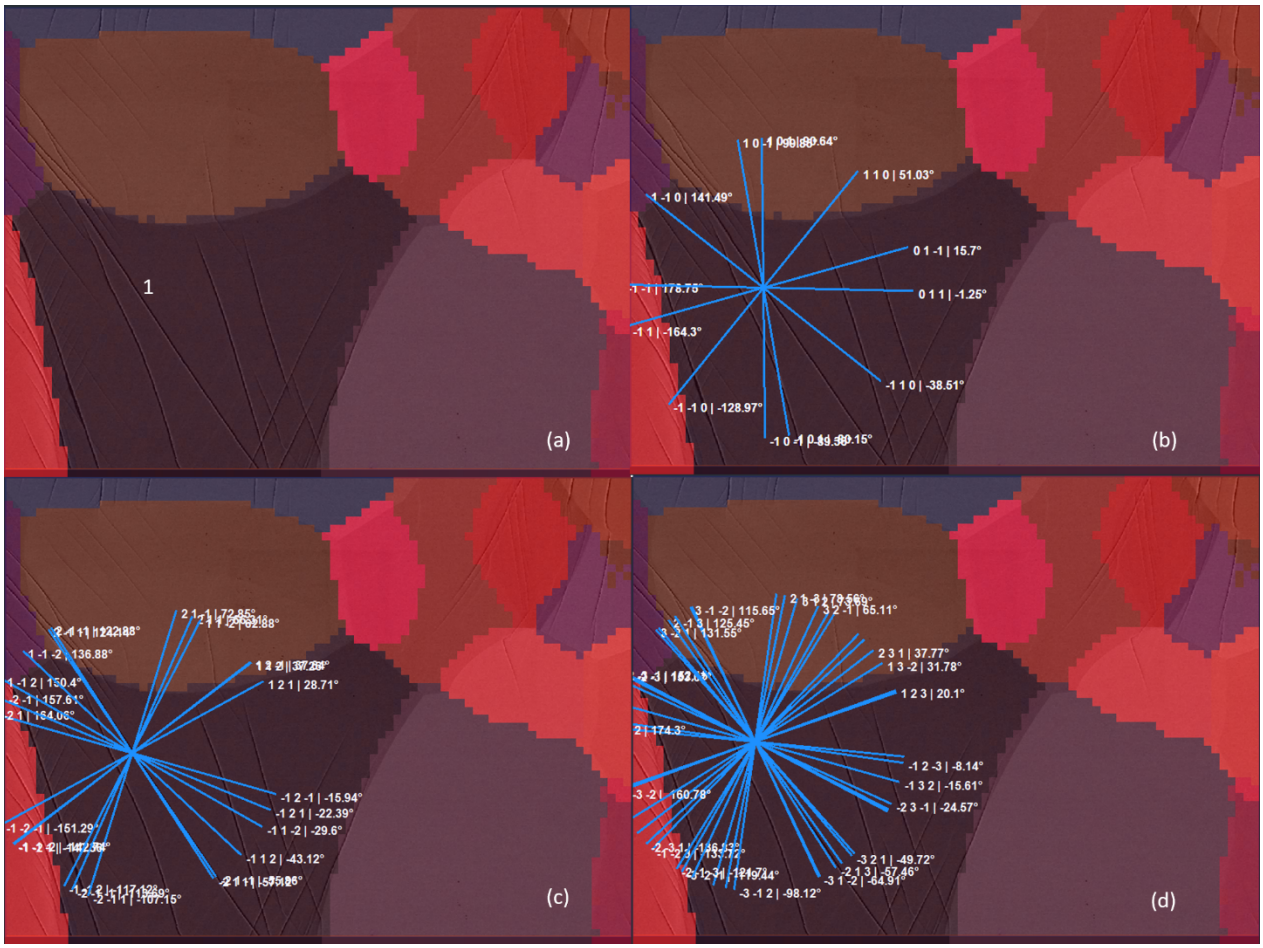

An example of slip trace analysis for line 1 using ATEX, shown in (a) and the corresponding slip traces for (b) {110}, (c) {112} and (d) {123} family of planes, showing an ambiguity between the {112} and {123} family of slip planes for slip line 1.

To account for such ambiguities, a modified correlation vector is defined as follows:

$$\begin{pmatrix} R_1 \\ R_2 \\ R_3 \end{pmatrix} = \left| \begin{pmatrix} r_1 \\ r_2 \\ r_3 \end{pmatrix} - \begin{pmatrix} \max(r_1, r_2, r_3) \\ \max(r_1, r_2, r_3) \\ \max(r_1, r_2, r_3) \end{pmatrix} \right| \tag{3}$$

This will set the best matching $R_i's (i = 1,2,3)$ to zero and others to some non-zero quantity. A threshold value has been defined for the R_i's such that one observed slip line can be attributed to two different slip families. For this study R_i was chosen to be < 0.001, as the threshold value can be defined based on the precision of orientation measurements

by EBSD, which has an upper bound of ~2° [53]. The value corresponding to R_i < 'threshold' is set to zero, thus classifying that particular line, 'i' as belonging to either two of the three possible slip systems.

Subsequent to this, a counting algorithm is formulated to quantify the slip family distribution in a given region of interest. According to the convention defined above, a detected slip line can belong to one of the six possible cases, as listed in Table 1. The slip trace matching procedure was carried out for nine points on each detected slip line (Figure 2(iii)). Each point on a detected slip line contributes to $\frac{1}{n}^{\text{th}}$ of the measurement count for cases 1,2 and 3, listed in Table 1. For cases 4,5 and 6 in Table 1, wherein there is an ambiguity between two slip families, each point contributes to $\frac{1}{2n}^{\text{th}}$ of the measurement count for the two ambiguous slip plane families.

	Slip plane family	**n{110}**	**n{112}**	**n{123}**
1	{110}	$\frac{1}{n}$		
2	{112}		$\frac{1}{n}$	
3	{123}			$\frac{1}{n}$
4	{110} or {112}	$\frac{1}{2n}$	$\frac{1}{2n}$	
5	{112} or {123}		$\frac{1}{2n}$	$\frac{1}{2n}$
6	{110} or {123}	$\frac{1}{2n}$		$\frac{1}{2n}$

Table 1: *Convention adopted to classify the detected slip line according to the six possible cases and the measurement count corresponding to each point on a detected slip line for*

the six possible cases. There çare n=9 points that are considered on a detected line in this study.

The total number of counts corresponding to each slip plane family, denoted by ($n(R_i)$), for n points on M slip lines detected in a given region of interest is given by:

$$\begin{pmatrix} N(R_1) \\ N(R_2) \\ N(R_3) \end{pmatrix} = \sum_{k=1}^{k=n\times M} \begin{pmatrix} n(R_1) \\ n(R_2) \\ n(R_3) \end{pmatrix}_k \tag{4}$$

The probability of observing a slip line corresponding to a given slip plane family $\mathcal{P}[N(R_i)]$ follows from the counting procedure defined above and is given by:

$$\mathcal{P}[N(R_i)]_{\text{for } i=1,2,3} = \frac{N(R_i)}{N(R_1)+N(R_2)+N(R_3)} \tag{5}$$

2.3 Crystal plasticity-based modelling:

In order to identify the relevant slip parameters associated with the slip-line statistics obtained from the automation procedure, a full-field crystal plasticity modelling routine was adopted in DAMASK using the basic scheme of the spectral solver variant [54], [55]. The continuum mechanical framework uses a multiplicative decomposition of the deformation gradient **F**:

$$\mathbf{F} = \frac{\partial \mathbf{y}}{\partial \mathbf{x}} = \mathbf{F_e F_p} \tag{6}$$

into elastic and plastic components ($\mathbf{F_e}$ and $\mathbf{F_p}$), with **x**, the co-ordinates in a reference configuration mapped onto the co-ordinates **y**, in the deformed configuration. The plastic velocity gradient $\mathbf{L_p}$ is related to the plastic deformation gradient $\mathbf{F_p}$ by:

$$\dot{\mathbf{F_p}} = \mathbf{L_p F_p} \tag{7}$$

The plastic velocity gradient $\mathbf{L_p}$ is calculated as the sum over the individual plastic shear rates $\dot{\boldsymbol{\gamma}}^{\boldsymbol{\varepsilon}}$ on each slip system ε = 1…….N, with N being the total slip systems across all considered slip families as follows:

$$\mathbf{L_p} = \sum_{\alpha} \dot{\boldsymbol{\gamma}}^{\boldsymbol{\varepsilon}} (\mathbf{m_s^{\varepsilon}} \otimes \mathbf{n_s^{\varepsilon}}) \tag{8}$$

with $\mathbf{m_s^{\varepsilon}}$ and $\mathbf{n_s^{\varepsilon}}$ being unit vectors along the shear direction and the shear plane normal. The resolved shear stress $\boldsymbol{\tau}^{\boldsymbol{\varepsilon}} = \mathbb{C}\left(\frac{\mathbf{F_e^T F_e - I}}{\mathbf{2}}\right) : \mathbf{m_s^{\varepsilon}} \otimes \mathbf{n_s^{\varepsilon}}$ drives the slip system ε; where $\mathbb{C}$ denotes a fourth order elasticity stiffness tensor.

Crystallographic slip evolution is modelled according to a simple phenomenological constitutive relationship, first described by Hutchinson [3] and later by Pierce [56]. The plastic shear resistances on each slip system g^{ε}, with the slip system pointer ε = 1…...N, starting from a value of g_0^{ε}, evolves according to the following law [3]:

$$\dot{g}^{\varepsilon} = \sum_{\zeta} q_{\varepsilon\zeta} h_0 \left| 1 - \frac{g^{\zeta}}{g_{\infty}^{\zeta}} \right|^{a} \operatorname{sgn}\left(1 - \frac{g^{\zeta}}{g_{\infty}^{\zeta}}\right) \left|\dot{\gamma}^{\zeta}\right| \tag{9}$$

where h_0 and a are the slip hardening parameters, representing the hardening slope and the hardening exponent, respectively. $q_{\varepsilon\zeta}$ represents the slip interaction parameters and is a measure of the latent hardening and g_{∞}^{ζ} represents the bounding slip resistances, per slip system family.

Given the current slip resistance values g^{ε}, the shear rate on each slip system evolves according to the following law:

$$\dot{\gamma}^{\varepsilon} = \dot{\gamma}_0 \left| \frac{\tau^{\varepsilon}}{g^{\varepsilon}} \right|^{n} \operatorname{sgn}(\tau^{\varepsilon}) \tag{10}$$

where the individual shear rates depend on the ratio of the applied shear stress to the current slip resistance, $\dot{\gamma}_0$ being the reference shear rate and n the stress exponent.

The phenomenological power law described above, has been incorporated for BCC-Ti, with slip system definitions for all three slip plane families {110}, {112} and {123}, as listed in the appendix.

The slip interaction parameters, $q_{\varepsilon\zeta}$ are a measure of latent hardening occurring due to the interaction among different slip systems, arising from the complex interaction between different dislocation configurations. The slip interaction matrix for the ½<111> {110} and the ½<111> {112} slip systems for BCC, incorporated in DAMASK are based on the values computed by Queyreau *et al* [7]. The interaction matrix values proposed in this study for the interaction between the ½<111> {110} and ½<111> {123} and the ½<111> {112} and the ½<111> {123} slip systems have been kept similar to the interaction matrix between the ½<111> {110} and the ½<111> {112} slip systems. The assumption has no strong effect in the present study as the experimental investigation was carried out at the onset of plasticity wherein hardening and the interactions between the different slip systems have not yet become significant.

2.4 Procedure for comparing the statistics of the automation procedure to the field output-based statistics derived from crystal-plasticity (CP) models:

This section elucidates the procedure to compare the results of the slip-family distribution statistics from the automation procedure (Section 2.2.1 and 2.2.2) to the field outputs from the full-field CP model. A MATLAB code was used to carry out this comparison procedure and the algorithm for the same has been described in Section 2.4.1. The procedure described in Section 2.4.1 forms the basis for the optimization of the input CP parameters such that the statistics obtained from the modelling procedure matches well the slip family distribution statistics observed experimentally. This optimization procedure for the input CP parameters has been described in Section 2.4.2.

2.4.1 Comparison of the accumulated plastic slip strain on a given slip system with the detected slip-line family:

The post-processing of the simulated region of interest after deformation, gives us the orientation, deformation gradient, the Cauchy stress tensor and the accumulated plastic slip strain values at each pixel location in the sample coordinate system. The accumulated plastic slip strain values are registered as an output for all the 48 slip systems at each pixel location within the simulated micro-structure. These slip strain values are sorted in a descending order and stored along with the slip system family number corresponding to the sorted values. As listed in the appendix, slip system numbers 1-12 belong to {110} family, slip system numbers 13-24 belong to the {112} family and slip system numbers 25-48 belong to the {123} family. The coordinates (i, j) for the end points and the intermediate points of all the detected lines from the automation procedure $(i_1, j_1\ to\ i_{n\times M}, j_{n\times M})$ for 'M' detected lines are stored as an array for the comparison with the plastic slip strain output from DAMASK. The slip system family numbers (1-48) that are active at pixel locations corresponding to the detected slip lines via the automation procedure are used to formulate a counting procedure. This is used to compare the results of the automation procedure to the slip system activity predicted by the model. Since the automated slip family detection procedure is able to distinguish the slip lines based on the traces of the active slip plane family and does not distinguish between different slip directions, no distinction is made between different slip directions in the counting procedure. The top 'r' values for the accumulated plastic slip strain are chosen such that these 'r' slip systems contribute to 99% of the cumulative plastic slip strain at the given location. The contribution from the top 'r' slip systems at a given pixel location can come from any of the 48 active slip systems. A weight function-based procedure is used for considering the contributions from the different active slip systems, as described below:

The contribution to the accumulated plastic slip strain from slip system 'ε '= 1……. r, is given by $\boldsymbol{\gamma^{\varepsilon}}$ and the cumulative plastic strain from the top 'r' systems is given by: $\sum_1^r \boldsymbol{\gamma^{\varepsilon}}$. The weight function associated with slip system 'ε 'is defined by:

$$w_{\varepsilon=1\ldots r} = \frac{\boldsymbol{\gamma^{\varepsilon}}}{\sum_1^r \boldsymbol{\gamma^{\varepsilon}}} \tag{11}$$

The weight function vector has 'r' components and the $r \times 1$ matrix for the pixel position (i, j) is given by:

$$\begin{bmatrix} w_{\varepsilon_1} \\ w_{\varepsilon_2} \\ \cdot \\ \cdot \\ w_{\varepsilon_r} \end{bmatrix}_{i,j}$$

The initial count of contribution of all three slip system families are defined as follows:

$$\begin{bmatrix} n_{\{110\}} \\ n_{\{112\}} \\ n_{\{123\}} \end{bmatrix}_{initial} = \begin{bmatrix} 0 \\ 0 \\ 0 \end{bmatrix}$$

The contribution from all three slip system families at each pixel position (i, j) corresponding to the detected slip line via the automation procedure is a $3 \times r$ matrix and is exemplified as follows:

$$\begin{matrix} & 1 & 2 & 3 & \ldots\ldots\ldots & k & \ldots\ldots\ldots & r \\ \{110\} \\ \{112\} \\ \{123\} \end{matrix} \begin{bmatrix} \frac{1}{n} & 0 & 0 & & 0 & & 0 \\ 0 & 0 & 0 & \ldots\ldots\ldots & \frac{1}{n} & \ldots\ldots\ldots & \frac{1}{n} \\ 0 & \frac{1}{n} & \frac{1}{n} & & 0 & & 0 \end{bmatrix}_{i,j}$$

The contribution to the k[th] column in the matrix defined above comes from one of the 'n' points on a detected slip line and hence gets counted as $\frac{1}{n}$. The non-zero matrix entry for the k[th] column corresponds to the contribution from the 'ε '= k[th] active slip system family at the given pixel position (i, j), indicated by the non-zero entry for the k[th] column. Slip system number 1-12 are counted in the {110} row, similarly for slip system numbers 13-24 and 25-48 are counted in the {112} and {123} rows, respectively. For example, if the

contribution to the k[th] column comes from the {112} family i.e; the slip system numbers 13-24, the matrix entry for the k[th] column is given by:

$$\begin{bmatrix} 0 \\ \frac{1}{n} \\ 0 \end{bmatrix}$$

The total counts corresponding to the contributions of the accumulated plastic slip strain from the active slip system families for all the detected points are computed as follows:

$$\begin{bmatrix} n_{\{110\}} \\ n_{\{112\}} \\ n_{\{123\}} \end{bmatrix}_{total} = \begin{bmatrix} n_{\{110\}} \\ n_{\{112\}} \\ n_{\{123\}} \end{bmatrix}_{initial} + \sum_{i_1,j_1}^{i_{n\times M},j_{n\times M}} \begin{bmatrix} \frac{1}{n} & 0 & 0 & & 0 & & 0 \\ 0 & 0 & 0 & \dots\dots\dots & \frac{1}{n} & \dots\dots\dots & \frac{1}{n} \\ 0 & \frac{1}{n} & \frac{1}{n} & & 0 & & 0 \end{bmatrix}_{i,j} \times$$

$$\begin{bmatrix} w_{\varepsilon_1} \\ w_{\varepsilon_2} \\ \cdot \\ \cdot \\ w_{\varepsilon_r} \end{bmatrix}_{i,j} \tag{12}$$

Next, the probabilities for different active slip families are computed, similar to the procedure introduced in the automation algorithm. The probability for a given slip family is computed from the $\begin{bmatrix} n_{\{110\}} \\ n_{\{112\}} \\ n_{\{123\}} \end{bmatrix}_{total}$ values, as follows:

$$\mathcal{P}_{\{110\}/\{112\}/\{123\}} = \frac{n_{\{110\}/\{112\}/\{123\}}}{n_{\{110\}} + n_{\{112\}} + n_{\{123\}}} \tag{13}$$

Finally, the slip family distribution as evidenced from the modelling routine is compared with the slip family distribution statistics observed experimentally.

2.4.2 Modelling parameters and identification of CRSS ratios from slip line statistics

Tensile tests were simulated under an iso-strain homogenization scheme [2] with an applied strain rate of 3.3×10^{-4} s^{-1}. The EBSD orientation data acquired from three different regions of interest were used as an input to digitize the microstructure, to be

used as an input geometry file under fully periodic boundary conditions in DAMASK. Uniaxial tension tests were simulated to a total strain of 0.5%, discretized into 100 time increments by setting the average deformation gradient and the complementary first PIOLA-KIRCHHOFF stress to

$$\frac{\langle \dot{\mathbf{F}} \rangle}{10^{-4}s^{-1}} = \begin{bmatrix} 3.3 & 0 & 0 \\ 0 & * & 0 \\ 0 & 0 & * \end{bmatrix} \text{ and } \frac{\langle \mathbf{P} \rangle}{Pa} = \begin{bmatrix} * & * & * \\ * & 0 & * \\ * & * & 0 \end{bmatrix}$$

The '*' symbol denotes tensor components that are free to evolve as per the applied boundary conditions. For the β-Ti21S polycrystal studied here, the single crystal elastic constants have been adopted from the previous work by Hounkpati *et al.* and Herbig *et al.* [38], [57]. The material parameters that express the strain rate sensitivity of the material has been adopted from the work of Lhadi *et al.* [58]. The initial set of input CRSS values for the three active slip systems, the other hardening parameters 'h_0' and 'a', defined in section 2.3, were taken from the work of Hounkpati *et al.* [57]. Owing to the lack of relevant data on the interaction parameters for different slip systems, a simplified interaction value has been used in this modelling routine to model the different types of slip system interactions. The self-interaction co-efficient has been taken to be 1 and the other latent hardening parameters are fixed to be 1.4. The initial set of CRSS values taken from the work of Hounkpati *et al.* were 310MPa for the {110} <111> slip system family, 330MPa for the {112} <111> slip system family and 350MPa for the {123} <111> slip system family. These values underestimated the experimentally observed yield stress in this study of ~795MPa. In their study, the yield stress was measured to be ~679MPa [57]. Hence the CRSS values were tuned to match the experimentally observed yield stress. The saturation stress τ_{sat} for all the three slip systems were kept to be the same as 800MPa. The material parameters used in this study have been tabulated in the *appendix*. Following the yield stress matching procedure, the CRSS ratios were systematically tuned

to match the slip family distribution statistics observed experimentally. At the onset of plasticity, the CRSS ratios play a dominant role in governing the distribution of plastic slip on different slip families as per a recent genetic algorithm base parametric study of the effect of various crystal plasticity parameters on the mechanical response of CP simulations [20]. The average CRSS value for the three slip systems, defined as $g_0^{avg} = \frac{g_0^{\{110\}} + g_0^{\{112\}} + g_0^{\{123\}}}{3}$, were kept to be the same for the different CRSS ratios to match the experimentally observed yield stress. The experimental probabilities for the region of interest is given by equation (5), $\mathcal{P}[\mathrm{N}(\mathrm{R_i})]_{\text{for i=1,2,3}}{}^{expt}$, and the probabilities for a given set of CRSS ratios, as obtained from DAMASK, are given by equation (13), $\mathcal{P}_{\{110\}/\{112\}/\{123\}}{}^{CRSS\ ratio\ (i)}$. The sum of least squared differences for the i[th] CRSS ratio is formulated as follows:

$$\chi_{SSD}^{CRSS\ ratio\ (i)} = \left[\mathcal{P}[\mathrm{N}(\mathrm{R_1})]^{expt} - \mathcal{P}_{\{110\}}{}^{CRSS\ ratio\ (i)}\right]^2 + \left[\mathcal{P}[\mathrm{N}(\mathrm{R_2})]^{expt} - \mathcal{P}_{\{112\}}{}^{CRSS\ ratio\ (i)}\right]^2 + \left[\mathcal{P}[\mathrm{N}(\mathrm{R_3})]^{expt} - \mathcal{P}_{\{123\}}{}^{CRSS\ ratio\ (i)}\right]^2 \quad (14)$$

We start with a CRSS ratio of 1:1:1 for all the three slip system families and progressively change the CRSS ratio to minimize the sum of least squared differences between the percentages of active slip families observed experimentally and from the modelling routine.

3 Results

3.1 Slip-line family distribution statistics:

The automated slip line detection algorithm, described in Section 2.2, was run for three deformed regions of interest and have been shown in Figure 4. The ECCI micrographs for three deformed regions of interest, superimposed on the EBSD maps from the same regions, are shown in Figure 4 (i), (ii) & (iii). The results of the automation algorithm

applied to these micrographs have been shown in Figure 4 (iv), (v) & (vi) and the corresponding pie-charts in Figure 4 (vii), (viii) & (ix). The majority of observed slip traces were observed to belong to the {123} family for all the three regions. It has been previously reported in literature that the activation of anomalous slip systems in BCC crystals is a strong function of composition [45]. The dominance of the {112} and the {123} slip system families was also observed for tensile experiments on α-Fe at room temperature [39], [40], [59]. These results would be interpreted in the light of the fact that the β-Ti21S polycrystal is compositionally different from previously reported studies on single crystalline BCC metals and in the current study, slip-line crystallography has been established at a meso-scale and hence these can be interpreted as 'apparent' slip planes, as observed during atomic-scale investigations on single crystals of Niobium by Douat *et al.* [60]. As concluded in the same study, it is possible that meso-scale slip-lines are composed of multiple atomic level {110} type slip steps.

The uncertainties in the pie-charts are estimated from Cochran statistics [61]. It is generally used for calculating the minimum sampling size (n_α) for a representative statistic:

$$\mathrm{n}_\alpha = \frac{\mathrm{Z}_C^2 \mathrm{p}_\alpha \mathrm{q}_\alpha}{\mathrm{m}_\alpha^2} \tag{15}$$

Where Z_C is the selected critical value of desired confidence level, C, obtained from the Z_C-score tables; p_α is the proportion of the glide plane family α according to the random distribution. Since there are 12 {110} type slip systems, 12 {112} type systems and 24 {123} type slip systems ($p_{\{123\}} = \frac{24}{48} = 0.5$; $p_{\{110\}} = p_{\{112\}} = \frac{12}{48} = 0.25$); $q_\alpha = 1 - p_\alpha$ and m_α is the desired margin of error for the glide plane family α. The number of points that have been sampled in a given region of interest has been given in Table 2 and the uncertainties have been calculated based on the same.

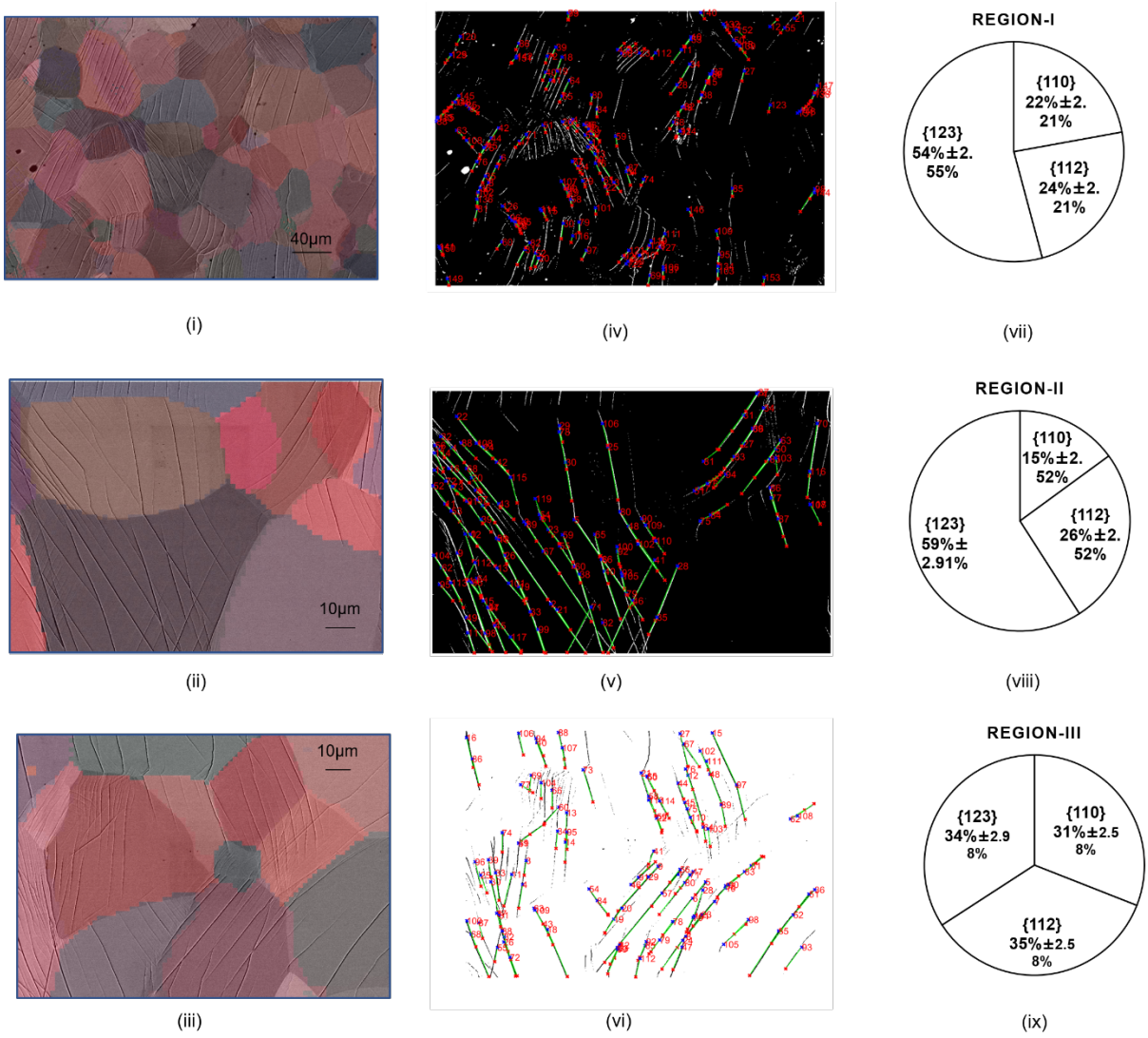

Figure 4: *Images (i) – (iii) are EBSD maps of the deformed region of interest with the ECCI micrographs of the slip traces superimposed on the EBSD maps. (iv), (v) and (vi) are the results from the automated slip line detection algorithm for these deformed regions and (vii), (viii) and (ix) are the slip family distributions obtained from these regions of interest.*

It is important to note that even though Regions-II and III have limited number of grains compared to Region-I, the number of points considered for sampling the slip distribution

is comparable to Region-I, which makes the slip distribution from these areas statistically relevant.

	No. of grains	No. of detected lines	No. of points considered for statistics
Region-I	55	153	1377
Region-II	12	119	1071
Region-III	14	114	1026

Table 2*: For the three regions analyzed in Figure 4, the number of grains, the number of slip lines detected and the number of points for collecting the slip-family distribution statistics have been listed.*

The 1st and 2nd minimum angular difference between the detected lines and the traces from all three slip plane families for Region-II have been shown in Figure 5(i). A cumulative frequency plot has been shown for the same set of measurements in Figure 5(ii). For each line number, the data for the angular difference has been extracted from multiple points on the detected line. From Figure 5(ii), it is noted that ~80% of the detected lines have an angular difference lesser than 5.5° and the value for the second minimum angular difference for all detected lines are under 10˚. EBSD mapping provides absolute grain orientations to an accuracy of ~2° [53]. Hence, slip traces that lie within an angular deviation of 2° from the detected slip line fall under the ambiguous category. The threshold value of 0.001 has been defined in Section 2.2.2, to highlight cases where an ambiguity exists between the selection of two slip systems. The threshold value of 0.001 corresponds to cases where the angular difference between the 1st and 2nd minimum values ranges from 0.62°-1.75°, for the 1st minimum angular difference with the slip traces ranging from 1°-5°.

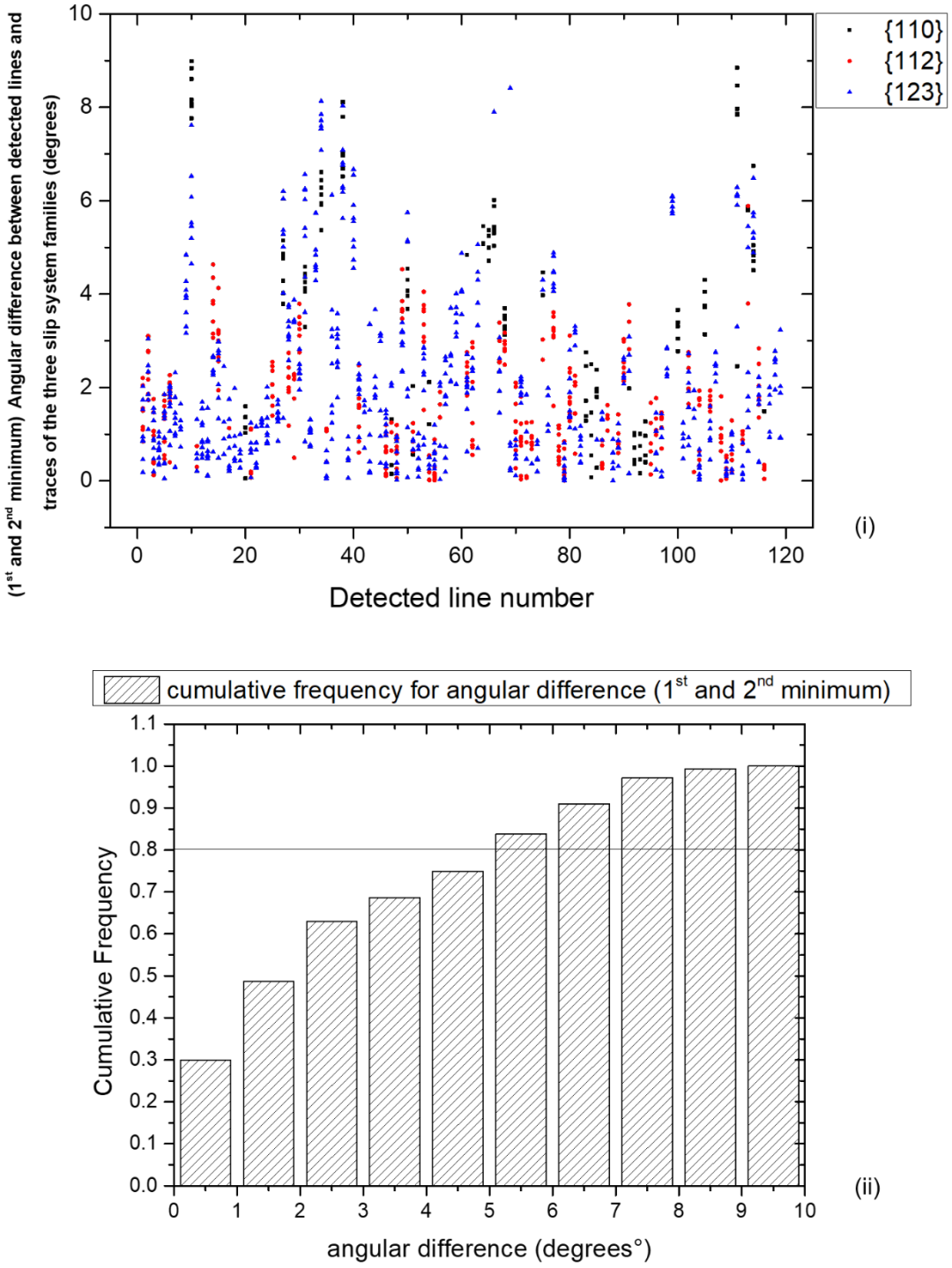

Figure 5: *Angular differences between the slope of the detected lines and the plane traces for all three slip families for Region-II. The 1st and 2nd minimum has been considered here, to show the range of the angular deviations with respect to all three slip system families.*

The modified correlation vectors $R_i's$, defined in section 2.2.2, have been plotted for the slip lines detected for Region-II, as shown in Figure 6. This plotting scheme projects the correlation vectors for the detected lines onto either one of the three planes; $R_1 - R_2$, $R_2 - R_3$or $R_1 - R_3$ or onto the R_1, R_2 *or* R_3 axis. For correlation vectors lying on either one of the three planes, the orthogonal vector component to the plane is zero and for these cases, we have only one slip system active. For correlation vectors lying on either one of the three axes, there are two correlation vector components that are zero and hence there exists an ambiguity for the slip-family selection in these cases.

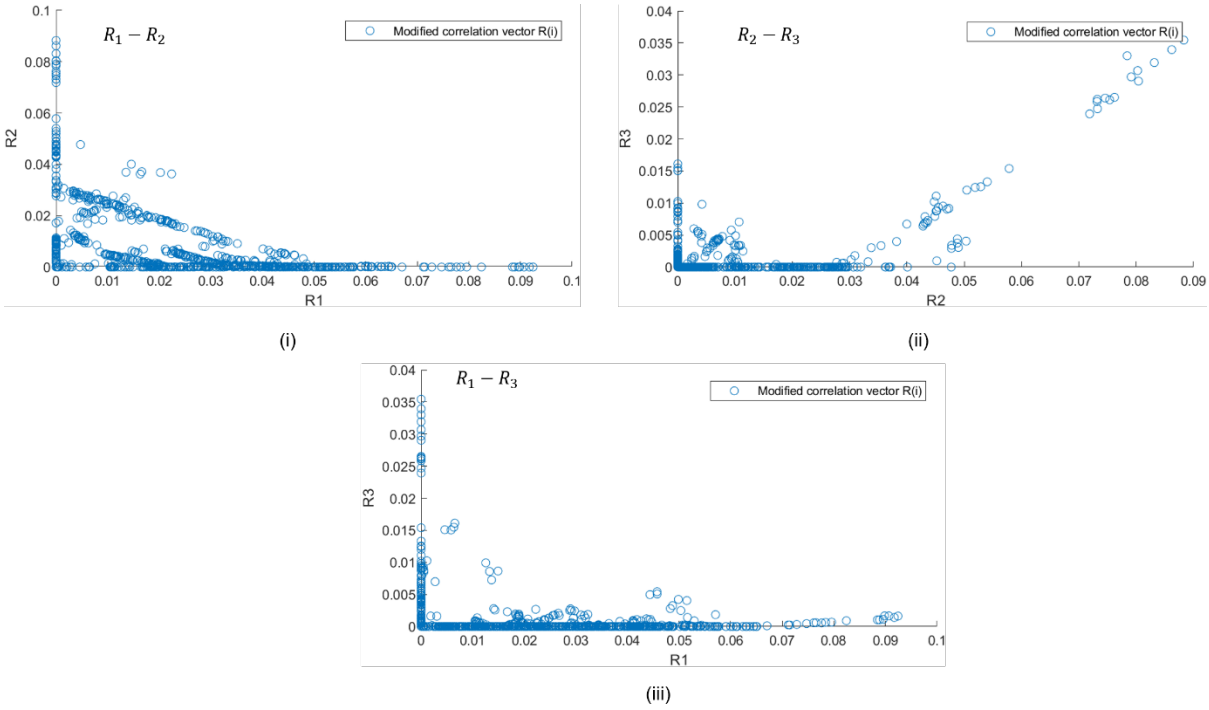

Figure 6: *Correlation vector plot (Equation 3, in section 2.2.2) for the detected slip lines from Region-II.*

The correlation vector plots for the different regions of interest are useful to visualize the consolidated information related to the slip family distribution and to track the evolution of the same as the material is loaded to a higher strain.

3.2 Comparison of the slip-line family distribution with accumulated plastic slip strain-based distribution from the crystal plasticity models:

The accumulated plastic slip strain distribution for Region-II has been shown in Figure 7(i). The slip system activity distribution was obtained from the locations where the slip traces were detected from the ECC micrographs. To obtain the χ_{SSD} maps, an initial CRSS value of 375 MPa was chosen for all three slip systems (ratio of 1:1:1), based on the experimental tensile yield stress matching procedure. The probabilities are computed according to equation (13) and the χ_{SSD} is computed according to equation (14). For the subsequent iterations, keeping the average CRSS for the three slip systems to be 375 MPa, the CRSS value for one slip system is reduced, as the reduction in CRSS for a given slip family increases the percentage contribution to plastic slip strain from that system. The CRSS ratios are tuned until a minimum χ_{SSD} value (0.005 or lower) is reached for all the three regions analyzed in this study. The slip distribution for the three regions (Figure 4) and the accumulated plastic slip strain-based distribution for the CRSS ratios with a minimum χ_{SSD} value are given in Table 3. It is to be noted that the slip-system family distribution from the model is compared to the ECCI based slip-distribution in an average sense for a given region. This is because at each pixel location for a detected slip line, the accumulated slip strain values for slip systems 1-48 are sorted in a descending order and the slip system families that contribute to 99% of the total cumulative slip strain are used to acquire the slip-distribution statistics from the crystal plasticity model. Thus, for each pixel location the contribution to the total slip strain comes from multiple slip system

families and their contribution to the slip system distribution is considered in weighted averaging scheme.

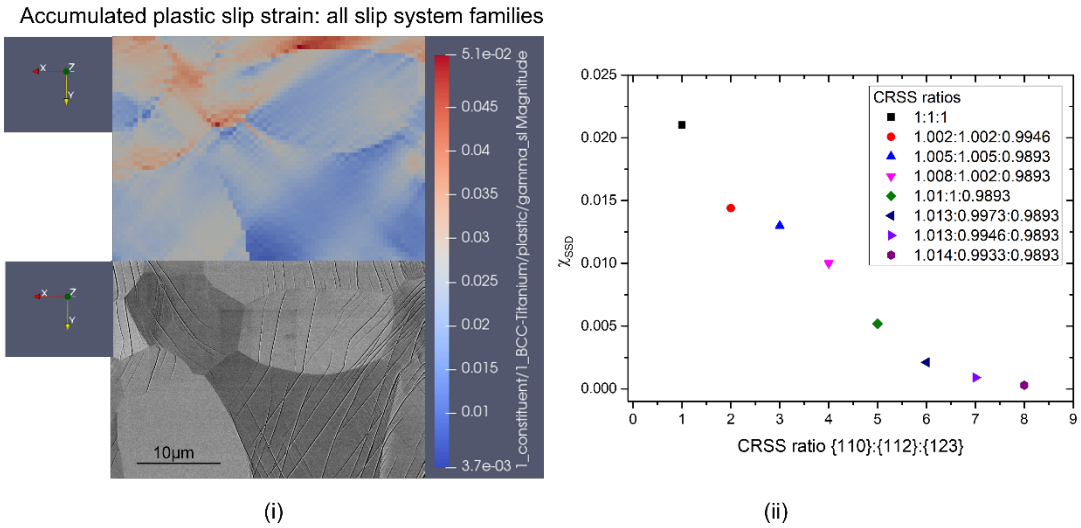

***Figure** 7: (i) The accumulated plastic slip distribution for all slip families compared to the slip-lines visible in the deformed region of interest (CRSS ratio - 1.014 :0.9933 :0.9893) (ii) Sum of squared difference, (χ_{SSD}) plot for different CRSS ratios calculated for Region-II.*

	Image-based slip distribution – Region I	**377:375:373 (1.005:1:0.9946)**	**Image-based slip distribution – Region II**	**380.5:372.5:371.0 (1.014 :0.9933 :0.9893)**	**Image-based slip distribution – Region III**	**375:369:381 (1 :0.984 :1.016)**
{110}	0.2214 ± 0.0221	0.2386 ± 0.0221	0.1495 ± 0.0252	0.1894 ± 0.0252	0.3096 ± 0.0258	0.3363 ± 0.0258
{112}	0.2369 ± 0.0221	0.2177 ± 0.0221	0.2597 ± 0.0252	0.215 ± 0.0252	0.3488 ± 0.0258	0.3089 ± 0.0258
{123}	0.5417 ± 0.0255	0.5437± 0.0255	0.5908 ± 0.0291	0.5956 ± 0.0291	0.3415 ± 0.0298	0.3548 ± 0.0298

***Table 3**: Image based slip-family distribution and the accumulated plastic slip-based distribution (highlighted in red) for the three regions analyzed in Figure 4 for CRSS ratios with a minimum χ_{SSD}. Unity corresponds to a CRSS value of 375 MPa.*

It is interesting to note that the CRSS values for which a minimum χ_{SSD} was obtained for the three regions are not very different from the initial value of 375 MPa, for which the best match with the yield stress was obtained. As the CRSS values are not very different from the uniform CRSS case, this possibly confirms the 'apparent slip plane' hypothesis that the observed {112} and {123} macroscopic slip-traces are made of multiple {110} slip traces at the microscopic level [47], [60], [62], but this is a preliminary hypothesis that needs experimental confirmation. Using the confrontational procedure discussed above, the slip line statistics from multiple regions on a given sample can be used to obtain a distribution of the CRSS ratios for which the best fit with the observed slip-line distribution statistics is obtained. Thus, macroscopic stress-strain plots can provide average CRSS values for the global description of poly-crystalline plasticity and the slip-family distribution matching procedure can give us local CRSS ratios, optimized according to the slip family statistics. However, since the statistics is based on slip-trace observation, the local slip density must be sufficient enough to cause sharp slip steps, which can be contrasted easily with the background micro-structure and ECCI is a promising technique to provide such high contrast slip line images.

4 Discussion

In this paper, we provide a method to automate slip trace analysis by using a Hough-transform based slip-line detection algorithm and thus provide a multiscale and statistical analysis of plastic slip activity in BCC β-Ti21S, particularly at the onset of plasticity. The results obtained have been confronted with a full-field CP modelling procedure executed

in DAMASK. We show that CP parameters, particularly the CRSS ratios, can be tuned to match the slip-family activity distribution observed locally, in addition to obtaining the best match for the macroscopic yield stress and thus this methodology provides good fitting parameters for a given CP model based on the slip-family distribution observed locally.

The *in situ* tensile test coupled with ECCI based microstructural characterization presents the advantage of providing high-contrast images of slip-lines for such an automation procedure to be used. Since it is possible to cover multiple regions of interest, it provides reliable statistics to obtain a distribution for input model parameters. The study reported here can also be applied to automate the detection of pencil glide systems in BCC and to investigate slip transfer mechanisms along grain boundaries at different strain states. As the statistical distributions are being obtained from multiple points on a detected slip line, this makes the data obtained statistically relevant. Moreover, the described method is adaptable for data mining processes and model parameter optimization using a variety of different techniques like genetic algorithms [15], [20] or Bayesian inference [21], [63], which are becoming increasingly popular tools for parameter estimation. This approach could also be coupled to Heaviside-DIC studies for quantifying the shear slip localizations and lattice rotations for different slip steps [64]–[66], thus providing a richer dataset for statistical confrontation.

Appendix

Slip-system definition for all the potential 48 slip systems incorporated in DAMASK for BCC-Ti.

Slip system number	Slip Direction	Slip plane normal
1	$[1\bar{1}1]$	(011)
2	$[\bar{1}\bar{1}1]$	(011)
3	$[111]$	$(0\bar{1}1)$
4	$[\bar{1}11]$	$(0\bar{1}1)$
5	$[\bar{1}11]$	(101)
6	$[\bar{1}\bar{1}1]$	(101)
7	$[111]$	$(\bar{1}01)$
8	$[1\bar{1}1]$	$(\bar{1}01)$
9	$[\bar{1}11]$	(110)
10	$[\bar{1}1\bar{1}]$	(110)
11	$[111]$	$(\bar{1}10)$
12	$[11\bar{1}]$	$(\bar{1}10)$
13	$[\bar{1}11]$	(211)
14	$[111]$	$(\bar{2}11)$
15	$[11\bar{1}]$	$(2\bar{1}1)$
16	$[1\bar{1}1]$	$(21\bar{1})$
17	$[1\bar{1}1]$	(121)
18	$[11\bar{1}]$	$(\bar{1}21)$
19	$[111]$	$(1\bar{2}1)$
20	$[\bar{1}11]$	$(12\bar{1})$
21	$[11\bar{1}]$	(112)
22	$[1\bar{1}1]$	$(\bar{1}12)$

23	$[\bar{1}11]$	$(1\bar{1}2)$
24	$[111]$	$(11\bar{2})$
25	$[11\bar{1}]$	(123)
26	$[1\bar{1}1]$	$(\bar{1}23)$
27	$[\bar{1}11]$	$(1\bar{2}3)$
28	$[111]$	$(12\bar{3})$
29	$[\bar{1}11]$	(312)
30	$[111]$	$(\bar{3}12)$
31	$[11\bar{1}]$	$(3\bar{1}2)$
32	$[1\bar{1}1]$	$(31\bar{2})$
33	$[1\bar{1}1]$	(231)
34	$[11\bar{1}]$	$(\bar{2}31)$
35	$[111]$	$(2\bar{3}1)$
36	$[\bar{1}11]$	$(23\bar{1})$
37	$[1\bar{1}1]$	(132)
38	$[11\bar{1}]$	$(\bar{1}32)$
39	$[111]$	$(1\bar{3}2)$
40	$[\bar{1}11]$	$(13\bar{2})$
41	$[11\bar{1}]$	(213)
42	$[1\bar{1}1]$	$(\bar{2}13)$
43	$[\bar{1}11]$	$(2\bar{1}3)$
44	$[111]$	$(21\bar{3})$
45	$[\bar{1}11]$	(321)
46	$[111]$	$(\bar{3}21)$
47	$[11\bar{1}]$	$(3\bar{2}1)$
48	$[1\bar{1}1]$	$(32\bar{1})$

Material parameters as defined in Section 2.3 for the DAMASK simulations

	Parameters
$C_{11}(GPa)$	153.0
$C_{12}(GPa)$	101.0
$C_{44}(GPa)$	57.0
$g_0^{\{110\}}(MPa)$	375 (first iteration) and then optimization by minimizing χ_{SSD}
$g_0^{\{112\}}(MPa)$	375 (first iteration) and then optimization by minimizing χ_{SSD}
$g_0^{\{123\}}(MPa)$	375 (first iteration) and then optimization by minimizing χ_{SSD}
$h_0\,(MPa)$	400
$\tau_{sat}\,(MPa)$	800
a	2.0
n	20
$q_{\varepsilon\varepsilon}q_{\varepsilon\zeta}$	1.0, 1.4
$\dot{\gamma}_0$	10^{-3}

Acknowledgments

The authors would like to thank Dr. Martin DIEHL and Prof. Dierk RAABE from Max-Planck-Institut für Eisenforschung, Germany for fruitful discussions and assistance with the DAMASK code. This work was supported by the French State through the program "Investment in the future" operated by the National Research Agency (ANR) and

referenced by ANR-11-LABEX-0008-01 (LabEx DAMAS) and was also supported by the Région Grand Est.

Compliance with ethical standards

The authors have no conflicts of interest to disclose and informed consent was not applicable.

References

[1] R. A. Lebensohn and A. D. Rollett, "Spectral methods for full-field micromechanical modelling of polycrystalline materials," *Comput. Mater. Sci.*, vol. 173, p. 109336, Feb. 2020, doi: 10.1016/j.commatsci.2019.109336.

[2] F. Roters *et al.*, "DAMASK – The Düsseldorf Advanced Material Simulation Kit for modeling multi-physics crystal plasticity, thermal, and damage phenomena from the single crystal up to the component scale," *Comput. Mater. Sci.*, vol. 158, pp. 420–478, Feb. 2019, doi: 10.1016/j.commatsci.2018.04.030.

[3] J.W.Hutchinson, "Bounds and self-consistent estimates for creep of polycrystalline materials," *Proc. R. Soc. London. A. Math. Phys. Sci.*, vol. 348, no. 1652, pp. 101–127, Feb. 1976, doi: 10.1098/rspa.1976.0027.

[4] W. Sellars, CM and Tegart, "Relationship between strength and structure in deformation at elevated temperatures," *Mem Sci Rev Met*, vol. 63, no. 9, 1966.

[5] K. Naumenko, A. Kutschke, Y. Kostenko, and T. Rudolf, "Multi-axial thermo-mechanical analysis of power plant components from 9–12% Cr steels at high temperature," *Eng. Fract. Mech.*, vol. 78, no. 8, pp. 1657–1668, May 2011, doi: 10.1016/j.engfracmech.2010.12.002.

[6] B. F. Dyson and M. McLean, “Micromechanism-Quantification for Creep Constitutive Equations,” 2001, pp. 3–16.

[7] S. Queyreau, G. Monnet, and B. Devincre, “Slip systems interactions in α-iron determined by dislocation dynamics simulations,” *Int. J. Plast.*, vol. 25, no. 2, pp. 361–377, Feb. 2009, doi: 10.1016/j.ijplas.2007.12.009.

[8] R. Madec and L. P. Kubin, “Dislocation Interactions and Symmetries in BCC Crystals,” 2004, pp. 69–78.

[9] D. Raabe, M. Sachtleber, Z. Zhao, F. Roters, and S. Zaefferer, “Micromechanical and macromechanical effects in grain scale polycrystal plasticity experimentation and simulation,” *Acta Mater.*, vol. 49, no. 17, pp. 3433–3441, Oct. 2001, doi: 10.1016/S1359-6454(01)00242-7.

[10] S. Breumier, S. Sao-Joao, A. Villani, M. Lévesque, and G. Kermouche, “High strain rate micro-compression for crystal plasticity constitutive law parameters identification,” *Mater. Des.*, vol. 193, p. 108789, Aug. 2020, doi: 10.1016/j.matdes.2020.108789.

[11] D. Raabe, D. Ma, and F. Roters, “Effects of initial orientation, sample geometry and friction on anisotropy and crystallographic orientation changes in single crystal microcompression deformation: A crystal plasticity finite element study,” *Acta Mater.*, vol. 55, no. 13, pp. 4567–4583, Aug. 2007, doi: 10.1016/j.actamat.2007.04.023.

[12] D. Ma *et al.*, “Crystal plasticity study of monocrystalline stochastic honeycombs under in-plane compression,” *Acta Mater.*, vol. 103, pp. 796–808, Jan. 2016, doi: 10.1016/j.actamat.2015.11.016.

[13] E. Renner, A. Bourceret, Y. Gaillard, F. Amiot, P. Delobelle, and F. Richard, "Identifiability of single crystal plasticity parameters from residual topographies in Berkovich nanoindentation on FCC nickel," *J. Mech. Phys. Solids*, vol. 138, p. 103916, May 2020, doi: 10.1016/j.jmps.2020.103916.

[14] A. Guery, F. Hild, F. Latourte, and S. Roux, "Identification of crystal plasticity parameters using DIC measurements and weighted FEMU," *Mech. Mater.*, vol. 100, pp. 55–71, Sep. 2016, doi: 10.1016/j.mechmat.2016.06.007.

[15] K. Sedighiani, M. Diehl, K. Traka, F. Roters, J. Sietsma, and D. Raabe, "An efficient and robust approach to determine material parameters of crystal plasticity constitutive laws from macro-scale stress–strain curves," *Int. J. Plast.*, vol. 134, p. 102779, Nov. 2020, doi: 10.1016/j.ijplas.2020.102779.

[16] C. Zambaldi, C. Zehnder, and D. Raabe, "Orientation dependent deformation by slip and twinning in magnesium during single crystal indentation," *Acta Mater.*, vol. 91, pp. 267–288, Jun. 2015, doi: 10.1016/j.actamat.2015.01.046.

[17] C. Zambaldi and D. Raabe, "Plastic anisotropy of γ-TiAl revealed by axisymmetric indentation," *Acta Mater.*, vol. 58, no. 9, pp. 3516–3530, May 2010, doi: 10.1016/j.actamat.2010.02.025.

[18] C. Zambaldi, Y. Yang, T. R. Bieler, and D. Raabe, "Orientation informed nanoindentation of α-titanium: Indentation pileup in hexagonal metals deforming by prismatic slip," *J. Mater. Res.*, vol. 27, no. 1, pp. 356–367, Jan. 2012, doi: 10.1557/jmr.2011.334.

[19] H. Li, D. E. Mason, T. R. Bieler, C. J. Boehlert, and M. A. Crimp, "Methodology for estimating the critical resolved shear stress ratios of α-phase Ti using EBSD-

based trace analysis," *Acta Mater.*, vol. 61, no. 20, pp. 7555–7567, Dec. 2013, doi: 10.1016/j.actamat.2013.08.042.

[20] R. Bandyopadhyay, V. Prithivirajan, and M. D. Sangid, "Uncertainty Quantification in the Mechanical Response of Crystal Plasticity Simulations," *JOM*, vol. 71, no. 8, pp. 2612–2624, Aug. 2019, doi: 10.1007/s11837-019-03551-3.

[21] A. Mangal and E. A. Holm, "Applied machine learning to predict stress hotspots I: Face centered cubic materials," *Int. J. Plast.*, vol. 111, pp. 122–134, Dec. 2018, doi: 10.1016/j.ijplas.2018.07.013.

[22] S. Papanikolaou, M. Tzimas, A. C. E. Reid, and S. A. Langer, "Spatial strain correlations, machine learning, and deformation history in crystal plasticity," *Phys. Rev. E*, vol. 99, no. 5, p. 053003, May 2019, doi: 10.1103/PhysRevE.99.053003.

[23] U. Ali, W. Muhammad, A. Brahme, O. Skiba, and K. Inal, "Application of artificial neural networks in micromechanics for polycrystalline metals," *Int. J. Plast.*, vol. 120, pp. 205–219, Sep. 2019, doi: 10.1016/j.ijplas.2019.05.001.

[24] H. KRIAA, A. GUITTON, and N. MALOUFI, "Modeling Dislocation Contrasts Obtained by Accurate-Electron Channeling Contrast Imaging for Characterizing Deformation Mechanisms in Bulk Materials," *Materials (Basel).*, vol. 12, no. 10, p. 1587, May 2019, doi: 10.3390/ma12101587.

[25] S. Wei and C. C. Tasan, "Deformation faulting in a metastable CoCrNiW complex concentrated alloy: A case of negative intrinsic stacking fault energy?," *Acta Mater.*, vol. 200, pp. 992–1007, Nov. 2020, doi:

10.1016/j.actamat.2020.09.056.

[26] A. Vilalta-Clemente *et al.*, “Cross-correlation based high resolution electron backscatter diffraction and electron channelling contrast imaging for strain mapping and dislocation distributions in InAlN thin films,” *Acta Mater.*, vol. 125, pp. 125–135, Feb. 2017, doi: 10.1016/j.actamat.2016.11.039.

[27] R. D. Kerns, S. Balachandran, A. H. Hunter, and M. A. Crimp, “Ultra-high spatial resolution selected area electron channeling patterns,” *Ultramicroscopy*, vol. 210, p. 112915, Mar. 2020, doi: 10.1016/j.ultramic.2019.112915.

[28] J. Guyon, H. Mansour, N. Gey, M. A. Crimp, S. Chalal, and N. Maloufi, “Sub-micron resolution selected area electron channeling patterns,” *Ultramicroscopy*, vol. 149, pp. 34–44, Feb. 2015, doi: 10.1016/j.ultramic.2014.11.004.

[29] M. T. Welsch, M. Henning, M. Marx, and H. Vehoff, “Measuring the Plastic Zone Size by Orientation Gradient Mapping (OGM) and Electron Channeling Contrast Imaging (ECCI),” *Adv. Eng. Mater.*, vol. 9, no. 1–2, pp. 31–37, Feb. 2007, doi: 10.1002/adem.200600195.

[30] H. Kriaa, A. Guitton, and N. Maloufi, “Fundamental and experimental aspects of diffraction for characterizing dislocations by electron channeling contrast imaging in scanning electron microscope,” *Sci. Rep.*, vol. 7, no. 1, p. 9742, Dec. 2017, doi: 10.1038/s41598-017-09756-3.

[31] H. Mansour, J. Guyon, M. A. Crimp, N. Gey, B. Beausir, and N. Maloufi, “Accurate electron channeling contrast analysis of dislocations in fine grained bulk materials,” *Scr. Mater.*, vol. 84–85, pp. 11–14, Aug. 2014, doi: 10.1016/j.scriptamat.2014.03.001.

[32] M. Ben Haj Slama, N. Maloufi, J. Guyon, S. Bahi, L. Weiss, and A. Guitton, “In Situ Macroscopic Tensile Testing in SEM and Electron Channeling Contrast Imaging: Pencil Glide Evidenced in a Bulk β-Ti21S Polycrystal,” *Materials (Basel).*, vol. 12, no. 15, p. 2479, Aug. 2019, doi: 10.3390/ma12152479.

[33] M. BEN HAJ SLAMA *et al.*, “Electron Channeling Contrast Imaging characterization and crystal plasticity modelling of dislocation activity in Ti21S bcc material,” *Materialia*, p. 100996, 2020, doi: 10.1016/j.mtla.2020.100996.

[34] R. Kolli and A. Devaraj, “A Review of Metastable Beta Titanium Alloys,” *Metals (Basel).*, vol. 8, no. 7, p. 506, Jun. 2018, doi: 10.3390/met8070506.

[35] J. D. Cotton *et al.*, “State of the Art in Beta Titanium Alloys for Airframe Applications,” *JOM*, vol. 67, no. 6, pp. 1281–1303, Jun. 2015, doi: 10.1007/s11837-015-1442-4.

[36] R. Welsh, G and Boyer, “Materials property handbook: titanium alloys,” *ASM Int.*, pp. 1051–60, 1994.

[37] R. R. Boyer, “Titanium and Its Alloys: Metallurgy, Heat Treatment and Alloy Characteristics,” in *Encyclopedia of Aerospace Engineering*, Chichester, UK: John Wiley & Sons, Ltd, 2010.

[38] M. Herbig, “3D short fatigue crack investigation in beta titanium alloys using phase and diffraction contrast tomography,” INSA de Lyon, 2011.

[39] G. I. Taylor and C. F. Elam, “The Distortion of Iron Crystals,” *Proc. R. Soc. London. Ser. A, Contain. Pap. a Math. Phys. Character*, vol. 112, no. 761, pp. 337–361, Oct. 1926.

[40] W. Fahrenhorst and E. Schmid, “Über die plastische Dehnung von α-Eisenkristallen,” *Zeitschrift für Phys.*, vol. 78, no. 5–6, pp. 383–394, May 1932, doi: 10.1007/BF01342203.

[41] J. W. Christian, “Some surprising features of the plastic deformation of body-centered cubic metals and alloys,” *Metall. Trans. A*, vol. 14, no. 7, pp. 1237–1256, Jul. 1983, doi: 10.1007/BF02664806.

[42] M. S. Duesbery, “On non-glide stresses and their influence on the screw dislocation core in body-centred cubic metals I. The Peierls stress,” *Proc. R. Soc. London. A. Math. Phys. Sci.*, vol. 392, no. 1802, pp. 145–173, Mar. 1984, doi: 10.1098/rspa.1984.0027.

[43] Z. S. B. M. S. Duesbery, “On non-glide stresses and their influence on the screw dislocation core in body-centred cubic metals. II. The core structure,” *Proc. R. Soc. London. A. Math. Phys. Sci.*, vol. 392, no. 1802, pp. 175–197, Mar. 1984, doi: 10.1098/rspa.1984.0028.

[44] L. Dezerald, D. Rodney, E. Clouet, L. Ventelon, and F. Willaime, “Plastic anisotropy and dislocation trajectory in BCC metals,” *Nat. Commun.*, vol. 7, no. 1, p. 11695, Sep. 2016, doi: 10.1038/ncomms11695.

[45] C. R. M. Marichal, “Plasticity in bcc single crystals investigated by Laue diffraction during micro-compression,” EPFL PP - Lausanne.

[46] M. S. Duesbery and V. Vitek, “Plastic anisotropy in b.c.c. transition metals,” *Acta Mater.*, vol. 46, no. 5, pp. 1481–1492, Mar. 1998, doi: 10.1016/S1359-6454(97)00367-4.

[47] C. Marichal, H. Van Swygenhoven, S. Van Petegem, and C. Borca, "{110} Slip with {112} slip traces in bcc Tungsten," *Sci. Rep.*, vol. 3, no. 1, p. 2547, Dec. 2013, doi: 10.1038/srep02547.

[48] B. Peeters, S. R. Kalidindi, P. Van Houtte, and E. Aernoudt, "A crystal plasticity based work-hardening/softening model for b.c.c. metals under changing strain paths," *Acta Mater.*, vol. 48, no. 9, pp. 2123–2133, May 2000, doi: 10.1016/S1359-6454(00)00047-1.

[49] D. Raabe, "Simulation of rolling textures of b.c.c. metals considering grain interactions and crystallographic slip on {110}, {112} and {123} planes," *Mater. Sci. Eng. A*, vol. 197, no. 1, pp. 31–37, Jun. 1995, doi: 10.1016/0921-5093(94)09770-4.

[50] C. A. Schneider, W. S. Rasband, and K. W. Eliceiri, "NIH Image to ImageJ: 25 years of image analysis," *Nat. Methods*, vol. 9, no. 7, pp. 671–675, Jul. 2012, doi: 10.1038/nmeth.2089.

[51] L. G. Shapiro and G. C. Stockman, *Computer Vision*. Prentice Hall, 2001.

[52] J. Beausir, B and Fundenberger, "Analysis tools for electron and X-ray diffraction," *ATEX-software, Univ. Lorraine-Metz*, 2017.

[53] F. J. Humphreys, "Review Grain and subgrain characterisation by electron backscatter diffraction," *J. Mater. Sci.*, vol. 36, no. 16, pp. 3833–3854, 2001, doi: 10.1023/A:1017973432592.

[54] J.W.Hutchinson, "Numerically robust spectral methods for crystal plasticity simulations of heterogeneous materials," *Int. J. Plast.*, vol. 66, pp. 31–45, Mar.

2015, doi: 10.1016/j.ijplas.2014.02.006.

[55] P. Eisenlohr, M. Diehl, R. A. Lebensohn, and F. Roters, “A spectral method solution to crystal elasto-viscoplasticity at finite strains,” *Int. J. Plast.*, vol. 46, pp. 37–53, Jul. 2013, doi: 10.1016/j.ijplas.2012.09.012.

[56] D. Peirce, R. J. Asaro, and A. Needleman, “An analysis of nonuniform and localized deformation in ductile single crystals,” *Acta Metall.*, vol. 30, no. 6, pp. 1087–1119, Jun. 1982, doi: 10.1016/0001-6160(82)90005-0.

[57] V. Hounkpati *et al.*, “In situ neutron measurements and modelling of the intergranular strains in the near-β titanium alloy Ti-β21S,” *Acta Mater.*, vol. 109, pp. 341–352, May 2016, doi: 10.1016/j.actamat.2016.02.065.

[58] S. Lhadi, S. Berbenni, N. Gey, T. Richeton, and L. Germain, “Micromechanical modeling of the effect of elastic and plastic anisotropies on the mechanical behavior of β-Ti alloys,” *Int. J. Plast.*, vol. 109, pp. 88–107, Oct. 2018, doi: 10.1016/j.ijplas.2018.05.010.

[59] F. Sauerwald and H. G. Sossinka, “Über Sprödigkeit, Plastizität und die Gleitelemente des α-Eisens,” *Zeitschrift für Phys.*, vol. 82, no. 9–10, pp. 634–643, Sep. 1933, doi: 10.1007/BF01338335.

[60] B. Douat, C. Coupeau, J. Bonneville, M. Drouet, L. Vernisse, and L. Kubin, “Atomic-scale insight into non-crystallographic slip traces in body-centred cubic crystals,” *Scr. Mater.*, vol. 162, pp. 292–295, Mar. 2019, doi: 10.1016/j.scriptamat.2018.10.032.

[61] William G. Cohran and G. M. Cox, *Experimental Designs*. Wiley.

[62] C. Marichal *et al.*, “Origin of Anomalous Slip in Tungsten,” *Phys. Rev. Lett.*, vol. 113, no. 2, p. 025501, Jul. 2014, doi: 10.1103/PhysRevLett.113.025501.

[63] A. Rovinelli, M. D. Sangid, H. Proudhon, and W. Ludwig, “Using machine learning and a data-driven approach to identify the small fatigue crack driving force in polycrystalline materials,” *npj Comput. Mater.*, vol. 4, no. 1, p. 35, Dec. 2018, doi: 10.1038/s41524-018-0094-7.

[64] J. C. Stinville *et al.*, “Measurement of elastic and rotation fields during irreversible deformation using Heaviside-digital image correlation,” *Mater. Charact.*, vol. 169, p. 110600, Nov. 2020, doi: 10.1016/j.matchar.2020.110600.

[65] Y. Mammadi *et al.*, “Nanometric metrology by FIB-SEM-DIC measurements of strain field and fracture separation on composite metallic material,” *Mater. Des.*, vol. 192, p. 108665, Jul. 2020, doi: 10.1016/j.matdes.2020.108665.

[66] F. Bourdin *et al.*, “Measurements of plastic localization by heaviside-digital image correlation,” *Acta Mater.*, vol. 157, pp. 307–325, 2018, doi: 10.1016/j.actamat.2018.07.013.